AGU PUBLICATIONS

JGR

Journal of Geophysical Research: Solid Earth

RESEARCH ARTICLE
10.1002/2013JB010735

**Key Points:**
- Predicted seismic anisotropy of plumes relates variably to mantle flow and strain
- Fast direction of S wave splitting predicted to be perpendicular to plume flow
- Geodynamic models of S wave splits at the Eifel, Hawaiian, and Iceland hot spots

**Correspondence to:**
G. Ito,
gito@hawaii.edu

**Citation:**
Ito, G., R. Dunn, A. Li, C. J. Wolfe, A. Gallego, and Y. Fu (2014), Seismic anisotropy and shear wave splitting associated with mantle plume-plate interaction, *J. Geophys. Res. Solid Earth*, *119*, doi:10.1002/2013JB010735.

Received 2 OCT 2013
Accepted 18 MAY 2014
Accepted article online 21 MAY 2014

# Seismic anisotropy and shear wave splitting associated with mantle plume-plate interaction

**Garrett Ito[1], Robert Dunn[1], Aibing Li[2], Cecily J. Wolfe[3], Alejandro Gallego[1], and Yuanyuan Fu[4]**

[1]Department of Geology and Geophysics, SOEST, University of Hawai'i at Mānoa, Honolulu, Hawaii, USA, [2]Department of Earth and Atmospheric Sciences, University of Houston, Houston, Texas, USA, [3]Hawaiian Institute of Geophysics and Planetology, SOEST, University of Hawai'i at Mānoa, Honolulu, Hawaii, USA, [4]Institute of Earthquake Science, China Earthquake Administration, Beijing, China

**Abstract** Geodynamic simulations of the development of lattice preferred orientation in the flowing mantle are used to characterize the seismic anisotropy and shear wave splitting (SWS) patterns expected for the interaction of mantle plumes and lithospheric plates. Models predict that in the deeper part of the plume layer ponding beneath the plate, olivine *a* axes tend to align perpendicular to the radially directed plume flow, forming a circular pattern reflecting circumferential stretching. In the shallower part of the plume layer, plate shear is more important and the *a* axes tend toward the direction of plate motion. Predicted SWS over intraplate plumes reflects the asymmetric influence of plate shear with fast *S* wave polarization directions forming a pattern of nested U shapes that open in the direction opposing both plate motion and the parabolic shape often used to describe the flow lines of the plume. Predictions explain SWS observations around the Eifel hot spot with an eastward, not westward, moving Eurasian plate, consistent with global studies that require relatively slow net (westward) rotation of all of the plates. SWS at the Hawaiian hot spot can be explained by the effects of plume-plate interaction, combined with fossil anisotropy in the Pacific lithosphere. In ridge-centered plume models, the fast polarization directions angle diagonally toward the ridge axis when the plume is simulated as having low viscosity beneath the thermal lithosphere. Such a model better explains SWS observations in northeast Iceland than a model that incorporates a high-viscosity layer due to dehydration of the shallow-most upper mantle.

## 1. Introduction

Seismic anisotropy in the mantle is often attributed to deformation-induced lattice preferred orientation (LPO) of common anisotropic minerals, such as olivine and enstatite [e.g., *Nicholas and Christensen*, 1987], and therefore provides a means of remotely sensing mantle deformation. Regional studies of major hot spots, for example, have investigated geographic variations in depth-integrated, mantle anisotropy structure using shear wave splitting (SWS). The observations have been variously interpreted as revealing fossil LPO in the lithosphere [*Collins et al.*, 2012], shearing of the ductile upper mantle by absolute plate motion [*Bjarnason et al.*, 2002; *Li and Detrick*, 2003; *Waite et al.*, 2005], flow associated with the interaction between a mantle plume and the overlying plate(s) [*Walker et al.*, 2005; *Xue and Allen*, 2005], or some combination thereof [*Fontaine et al.*, 2005, 2007; *Barruol and Fontaine*, 2013].

The underpinning assumption guiding the above interpretations is that the seismically fast, olivine *a* axes (and the fast polarization direction of a vertically propagating *S* wave) align parallel to mantle flow. This assumption is adopted largely out of simplicity, even though it is known to apply only in the specific situation of large strain (e.g., $>\sim 150\%$) during simple shear (for dry olivine [*Jung and Karato*, 2001]), but not for most other deformation conditions [*Ribe*, 1989; *Wenk et al.*, 1991; *Zhang and Karato*, 1995]. Another simplifying assumption often invoked is that the olivine *a* axes tend to align with the direction of accumulated extensional strain [e.g., *Fischer et al.*, 2000; *Druken et al.*, 2013] or, equivalently, the long axis of the finite strain ellipsoid (FSE) [e.g., *Ribe*, 1992]. More recently, it has been shown that for general steady deformation, LPO in an olivine aggregate evolves such that the olivine *a* axes tend to align with neither the direction of flow nor accumulated extension but instead to the long axis of the FSE at infinite strain, or the infinite strain axis (ISA) [*Kaminski and Ribe*, 2002]. With time-dependent deformation, the *a* axes and ISA generally do not align, but how closely they do depends on how quickly LPO is developing relative to how quickly the ISA is changing direction [*Kaminski and Ribe*, 2002].

At the interior of plates, far ($>\sim 500$ km) from plate boundaries and hot spots, the fast polarization directions of SWS [*Conrad et al.*, 2007], the fast propagation directions of surface waves [*Gaboret et al.*, 2003], the long

axes of the FSE, and the olivine *a* axes [*Becker et al.*, 2006] are more likely to parallel the direction of upper mantle flow. However, where mantle deformation varies rapidly in space such as near-plate boundaries and hot spots, the relationships between the directions of mantle flow, the FSE, and LPO are expected to be complex and variable [*Kaminski and Ribe*, 2002]. Geodynamic models are thus needed for more realistic interpretations of SWS observations.

The purpose of this study is to characterize the expected patterns of mantle seismic anisotropy and shear wave splitting associated with mantle plume-plate interaction. Our methodology is to numerically compute mantle flow in three dimensions [*Moresi and Gurnis*, 1996; *Zhong et al.*, 2000], simulate the evolution of LPO for an olivine-enstatite aggregate [*Kaminski et al.*, 2004], produce synthetic shear wave splitting waveforms [*Rümpker and Silver*, 1998; *Fischer et al.*, 2000], and then invert for the splitting parameters [*Wolfe and Silver*, 1998]. Various cases of intraplate and ridge-centered plumes are examined. We then examine models of SWS at the Eifel, Hawaiian, and Iceland hot spots and present revised interpretations of the SWS observations.

## 2. Methods

### 2.1. Mantle Flow Calculations

Mantle flow due to plume-plate interaction was simulated by solving the equations governing conservation of mass, momentum, and energy in a Boussinesq fluid with zero Reynolds number and infinite Prandtl number using the finite element code Citcom [*Moresi and Gurnis*, 1996; *Zhong et al.*, 2000]. Stress is linearly related to strain rate by a viscosity that is an Arrhenius function of temperature and increases exponentially with pressure. In one model, viscosity also depends on mantle water content and hence increases by a factor of $10^2$ near the base of the melting zone as the mantle is dehydrated [*Hirth and Kohlstedt*, 1996], using the method of *Bianco et al.* [2013]. Cartesian geometry is used with *x* being aligned with plate motion (when applicable) and *z* being height above the model base (Figure 1). The models extend to 400 km depth, but the sizes of the finite elements vary so that the highest resolution is in the shallowest 200 km, within and surrounding the plume stem (Table 1 provides information about box dimensions and gridding).

The plume stem is imposed as a boundary condition at the base of the model with a fixed circular temperature anomaly that decays as a Gaussian function of radial distance from the center. The radius $r_p$ (set to 58–75 km) of the plume stem is the distance at which the excess temperature decays by $e^{-1}$. Otherwise, the model base has a reference potential temperature of 1350°C, has zero (nonhydrostatic) normal traction, and is open to flow across it. The boundary at $y = 0$ intersects the center of the plume and is a reflecting boundary (zero material or heat flow through and zero shear traction). The other side boundaries are either open or reflecting depending on the situation being simulated. Plate motion is imposed kinematically with the top surface moving at a specified rate (see Table 1 for more details).

### 2.2. Crystal Fabric Development and Seismic Anisotropy

The development of lattice preferred orientation (LPO) due to mantle flow was simulated using D-Rex (dynamic recrystallization-induced LPO) [*Kaminski and Ribe*, 2001; *Kaminski et al.*, 2004], an algorithm in which the deformation of individual grains of an olivine-enstatite aggregate is controlled kinematically by the imposed (and uncoupled) mantle flow. For each point in the model at which LPO was evaluated (every other finite element node), material was tracked backward along the material's flow line. Then starting with a system of $n = \sim 1300$ randomly oriented olivine (70%) and enstatite (30%) grains, the crystal aggregate was tracked forward in time through its full deformation history, along its flow line to its ending location. Deformation of the aggregate is accommodated by and LPO develops due to intracrystalline slip, dynamic recrystallization, and grain boundary sliding. Olivine displays different types of fabric, which depend on water content and strain rate, and are associated with different relationships between deformation and the preferred orientations of the three crystallographic axes [e.g., *Karato*, 2007]. We assume the A-type fabric (operant for low water contents) for simplicity and because it is probably most common in the upper mantle [*Karato*, 2007]. Because LPO develops due to dislocation creep, which probably dominates in the shallow upper mantle [e.g., *Karato and Wu*, 1993], we assume that LPO develops only at depths ≤200 km [*Karato*, 1992]. A Voigt average of the hexagonally symmetric, anisotropic elastic tensors of the *n* crystals was then taken to compute the bulk elastic tensor of the aggregate at each point in the model. The elastic tensors were then used to calculate radial anisotropy and shear wave splitting. Radial anisotropy is measured in the field using surface waves and defined

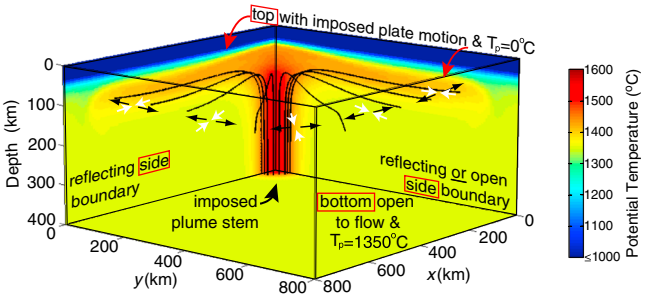


**Figure 1.** Three-dimensional perspective view of model box with boundary conditions described in labels. Solutions of potential temperature (colors) and flow lines (black curves) are for Model SP1 of an axisymmetric plume beneath a stationary lithospheric plate. Small arrows depict radial contraction (white) and circumferential extension (black) in the middle-to-deep part of the plume layer.

here as the ratio of the velocities of vertically to horizontally polarized *S* waves $V_{SV}/V_{SH} = (L/N)^{1/2}$, where *L* and *N* are functions of the elasticity tensor [*Takeuchi and Saito*, 1972].

### 2.3. Synthetic Shear Wave Splitting

Comparisons of model results to observations at hot spots are based on SWS predictions. Split *S* waveforms were calculated from the model anisotropy structure using the method of *Rümpker and Silver* [1998; see also *Fischer et al.*, 2000], in which splitting operators are applied consecutively to a vertically incident *S* wave to simulate the wave traveling through multiple anisotropic layers. The effects of each model layer (20 layers in the upper 200 km) were then integrated from bottom to top in order to compute the final waveform at the surface.

The synthetic waveforms were then used to solve for the appropriate splitting parameters beneath each model seismic station. The splitting parameters used for the main conclusions of the prior SWS studies of the Eifel [*Walker et al.*, 2005], Iceland [*Bjarnason et al.*, 2002; *Li and Detrick*, 2003; *Xue and Allen*, 2005], and Hawaiian [*Collins et al.*, 2012] hot spots were (i) polarization azimuth of the fast component $\phi$ and (ii) split time $\delta t$, both obtained by assuming a single anisotropic layer. In the above studies, solutions for $\phi$ and $\delta t$ were produced using *Silver and Chan*'s [1991] method, as modified by *Wolfe and Silver* [1998] to stack misfit functions for multiple *S* waves arriving at a given station (with different incident angles and polarization directions). While stacking removes any potential information about dipping olivine *a* axes or multilayer anisotropy, it provides a robust measure of the depth-averaged anisotropy beneath each station. For a direct comparison between our model predictions and the prior observations, we applied the same method to the synthetic waveforms.

The distributions of the initial polarizations of the model *SKS* waves were chosen to mimic the real distributions as determined by the back azimuths of the *SKS* phases used for each hot spot (model polarizations listed as counterclockwise angle from the model plate motion direction): Eifel [*Walker et al.*, 2005] (−35° to +35° in increments of 5°), Iceland [*Xue and Allen*, 2005] (83°, 91°, 99°, 107°, 115°, and 165°), and Hawaii [*Collins et al.*, 2012] (−3°, 5°, 13°, 21°, and 29°). Our comparisons between modeled and observed splitting focus on the agreement between fast polarization azimuths $\phi$, because we are most interested in the depth-averaged fast direction (rather than depth heterogeneity) and because solutions of $\phi$ are more robust in that the uncertainties tend to be proportionally lower than those for split time.

**Table 1.** Parameters of Mantle Flow Calculations

| Model Name | Model *x*, *y*, and *z* Dimensions (km) | Number of Finite Elements in *x*, *y*, and *z* | Rayleigh Number | Plume Radius[a] (km) | Peak Excess Plume Temperature | Plume Buoyancy Flux (Mg/s) | Plate Rate (km/Myr)[b] |
|---|---|---|---|---|---|---|---|
| SP1 | 1200 × 1200 × 400 | 192 × 192 × 64 | $1 \times 10^6$ | 65 | 200°C | 3.3 | 0.0 |
| SP2 | 1600 × 1000 × 400 | 256 × 160 × 64 | $1 \times 10^5$ | 75 | 200°C | 0.33 | 0.0 |
| IP1 | 1600 × 1000 × 400 | 256 × 160 × 64 | $1 \times 10^5$ | 75 | 200°C | 0.31 | 2.5 |
| IP2 | 1600 × 1000 × 400 | 256 × 160 × 64 | $1 \times 10^5$ | 75 | 200°C | 0.35 | 20 |
| IP3 | 1600 × 1000 × 400 | 256 × 160 × 64 | $1 \times 10^5$ | 75 | 200°C | 0.35 | 10 |
| IP4 | 1800 × 900 × 400 | 256 × 128 × 64 | $3.5 \times 10^5$ | 75 | 300°C | 3.8 | 90.0 |
| RC1 | 800 × 1200 × 400 | 128 × 192 × 64 | $1 \times 10^6$ | 65 | 200°C | 3.2 | 10.0 |
| RC2 | 800 × 1200 × 400 | 128 × 192 × 64 | $6 \times 10^5$ | 58 | 300°C | 2.3 | 1.0 |

[a]Plume temperature anomaly is a Gaussian function of radial distance from the plume center. Radius is the distance at which the excess temperature decays to 1/*e* of the peak.
[b]Rate of plate motion over an intraplate plume (IP1–IP5) or half the spreading rate for a ridge-centered plume (RC1 and RC2).

### 2.4. Comparison to Prior Studies and Model Limitations

A few geodynamic modeling studies have previously addressed, to various levels of sophistication, the relationships between mantle flow, seismic anisotropy, and seismic observables for mantle plumes. For example, *Rümpker and Silver* [2000] conducted a more extensive examination of SWS predictions than we do, especially by their considering the dependence on initial *S* wave polarization and incident angle. Their model of mantle anisotropy, however, was only conceptually defined (not formally computed by a geodynamic model) and limited to an ideal case of an axisymmetric plume rising beneath a stationary plate. Analog laboratory experiments by *Druken et al.* [2013] were advantageous in their ability to incorporate the full fluid-mechanical complexities of plumes interacting with both stationary and moving plates. The main weakness of their approach, compared to ours, is that their inferences of seismic anisotropy were limited by the simplified assumption that the direction of accumulated extension (measured using short filaments, or "whiskers," dispersed throughout the analog fluid) parallels the preferred orientation of the olivine *a* axes. *Marquart et al.*'s [2007] study of the mantle dynamics around the Iceland hot spot used numerical models of mantle convection and LPO development using D-Rex, much like we do here. However, their strategy differed in that the temperature structure in their simulations was derived from seismic tomography models, plate motion in their higher-resolution, regional model was not specified, and the comparison to observations relied on predicted orientations of the olivine *a* axes at select depth planes, rather than full predictions of SWS.

Our current study aims to advance the knowledge gained in the above studies by using more complete treatments of mantle flow, LPO development, seismic anisotropy, and predictions of SWS for comparisons with observations at select hot spots. Still, several limitations are worth acknowledging. First, a single method for predicting LPO (D-Rex) is used, whereas more mechanically consistent methods exist [e.g., see *Blackman*, 2007, and references therein] and are known to yield different results than D-Rex [*Castelnau et al.*, 2009]. In addition, whereas the assumption of the dry olivine (A-type) fabric may be relevant to many parts of the upper mantle, the possibility that plumes are not "dry" may mean that olivine textures develop differently beneath hot spots [*Karato*, 2007] than here simulated. Last, this study is limited to the effects of LPO induced by melt-free mantle flow. The presence of partial melt, however, can impact seismic anisotropy by altering the sense of strain accommodated by olivine [*Holtzman et al.*, 2003] or due to the presence of preferentially aligned melt channels [e.g., *Blackman and Kendall*, 1997; *Mainprice*, 1997; *Holtzman and Kendall*, 2010]. The understanding of each of the above issues is relatively immature, but as knowledge improves, so should the robustness of future model predictions.

## 3. Results: Intraplate Plume

### 3.1. Ideal Case of an Axisymmetric Plume Beneath a Stationary Plate

We first examine the idealistic case of an axisymmetric plume rising beneath a stationary plate (Figures 1 and 2). This model (Model SP1, Table 1) has reflecting side boundaries at $x = 0$ and $y = 0$; the plume is centered at $x = y = 0$, and so one quarter of a fully circular plume is simulated. The same situation was used for addressing SWS by *Fu et al.* [2012] and radial anisotropy by *Gallego et al.* [2013] and is presented again in this manuscript for building insight into subsequent models. Here the buoyant plume is predicted to rise vertically and then pond beneath the base of the lithosphere (~50 km depth) in a ~100-km-thick layer that spreads radially outward like a pancake (Figure 1). The anisotropy can be grouped into three main types (Table 2).

Type I is characterized by radial anisotropy in which $V_{SV}/V_{SH} > 1$ and weak SWS. Type I occurs primarily above the upwelling plume stem (radial distance < ~120 km) in the lower half of the plume pancake (depths of ~100–150 km). Here the flow is largely vertical, and the olivine *a* axes (represented by the direction of maximum *P* wave velocity, $V_p$ in Figure 2c) are predicted to tilt up and toward the plume center.

Type II is characterized by $V_{SV}/V_{SH} < 1$ and *a* axes that are oriented circumferentially around the center of the plume. Type II occurs around the plume stem over a wide range of radial distances near the bottom of the plume layer (e.g., $200 < r < 600$ km at 150 km depth, Figure 2b); it occurs over a more restricted range of distances at depths closer to the base of the lithosphere (e.g., $150 < r <$ ~250 km at 100 km depth, Figure 2a), and is essentially absent at the base of the lithosphere (not shown). For type II, LPO is controlled by vertical and radial contraction and circumferential stretching of the radially spreading plume pancake (Figure 1). Circumferential stretching is indicated by the orientations of the long axes of the finite strain ellipsoids (FSEs) in Figure 2. Thus, the *a* axes are perpendicular to the radial flow of the plume.

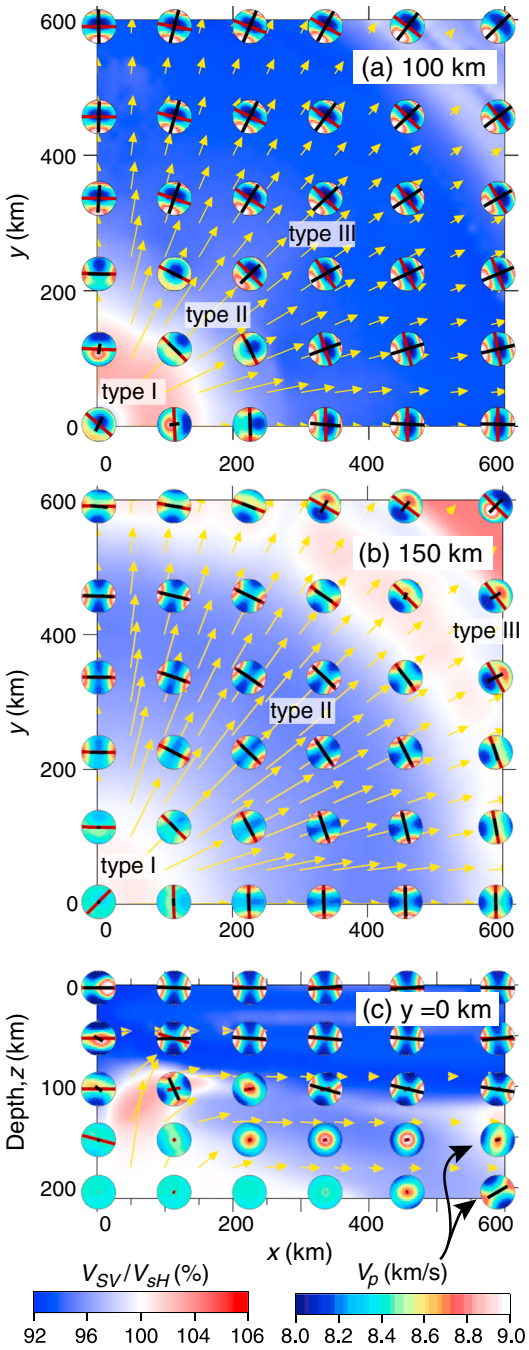


**Figure 2.** Anisotropy for Model SP1 in horizontal planes (a) near the base of the lithosphere (depth labeled), (b) in the middle of the spreading plume layer, and (c) in a vertical cross section at $y = 0$. The plume stem is centered at $(x, y) = (0, 0)$. Arrows indicate in-plane direction and magnitude of mantle flow. Radial anisotropy ($V_{SV}/V_{SH}$ in %) is shown as blue-white-red colors (left color bar); directional dependence of $P$ wave velocity, $V_P$, is shown by polar plots (outer hemispheres, right color bar). Black bars indicate direction of peak $V_P$, corresponding to the preferred orientation of olivine $a$ axes; red bars indicate direction of the long axis of the finite strain ellipsoid. In some locations the two bars plot on top of each other (e.g., everywhere $x < 400$ km, $y < 400$ km in Figure 2b), in other locations they differ (e.g., at $x = 600$, $y = 600$ in Figure 2b). Anisotropy types I–III (see Table 2) occur in the locations labeled in Figures 2a and 2b.

Type III is characterized by $V_{SV}/V_{SH} < 1$ and $a$ axes oriented radially, parallel to the direction of shear between the plume and plate. Type III occurs at $r > 600$ km near the base of the plume layer (Figure 2b) and $r >$ ~250 km in the shallower part of the plume layer (Figure 2a). For type III, LPO is dominated by shearing of the plume against the lithosphere. The switch from type II ($a$ axes circumferential) to type III ($a$ axes radial) indicates a switch from LPO being dominated by circumferential stretching to radial shear.

When shear wave splitting is calculated for the layer extending just from 200 to 100 km depth, fast polarization directions ($\phi$) are found to be oriented largely in a circular pattern around the plume center, perpendicular to mantle flow (Figure 3a), reflecting the type II anisotropy in the lower half of the plume pancake where circumferential stretching controls the LPO. When splitting is calculated at the surface, however, the fast directions are oriented radially (Figure 3b) as they are dominated by the type III anisotropy in the upper half of the plume pancake and in the slowly deforming lithosphere where radial shear is important.

These results demonstrate that the relationships between the directions of flow, accumulated extension, and the LPO can vary dramatically in space for even this simple, ideal case of a plume-plate interaction. The circumferential pattern of accumulated extension was also seen in laboratory experiments of plume-plate interaction [*Druken et al.*, 2013], which these authors assumed approximates the directions of the $a$ axes. However, like *Marquart et al.* [2007], we find that this assumption is appropriate in some, but not all, locations. Specifically, it is most appropriate within the deeper part of the plume pancake or near the plume stem where type II anisotropy occurs. But at shallower depths near the base of the lithosphere and farther from the plume stem, the $a$ axes are more heavily influenced by radial shear and become oriented radially, parallel to flow and perpendicular to the stretching direction (type III).

**Table 2.** Summary of Anisotropy Types Described in the Text

| Name | Defining Characteristics | Cause and Location |
|---|---|---|
| Type I | Fast $V_p$ axes (and olivine *a* axes) largely vertical; radial anisotropy ($V_{SV}/V_{SH}$) > 1 and weak SWS. | Vertical shear in the lower part of plume stem. |
| Type II | Fast $V_p$ axes oriented circumferentially around the plume stem; $V_{SV}/V_{SH} < 1$ and fast *S* wave polarization directions perpendicular to radial flow. | Circumferential stretching (and vertical and radial shortening) in lower half of plume pancake, surrounding the plume stem. |
| Type III | Fast $V_p$ axes tending toward the direction of plume-plate shear; $V_{SV}/V_{SH} \leq 1$ and fast polarization directions approaching or in the direction of plume-plate shear. | Plume-plate shear in the shallower part of the plume pancake. |
| Type IV | Horizontal components of fast $V_p$ oriented diagonally toward ridge axis; $V_{SV}/V_{SH} \leq 1$, fast polarization direction diagonal toward ridge axis. | Shear associated with along-axis plume flow (fastest beneath and decreasing away from ridge axis) and plate spreading near the ridge axis for a ridge-centered plume. |

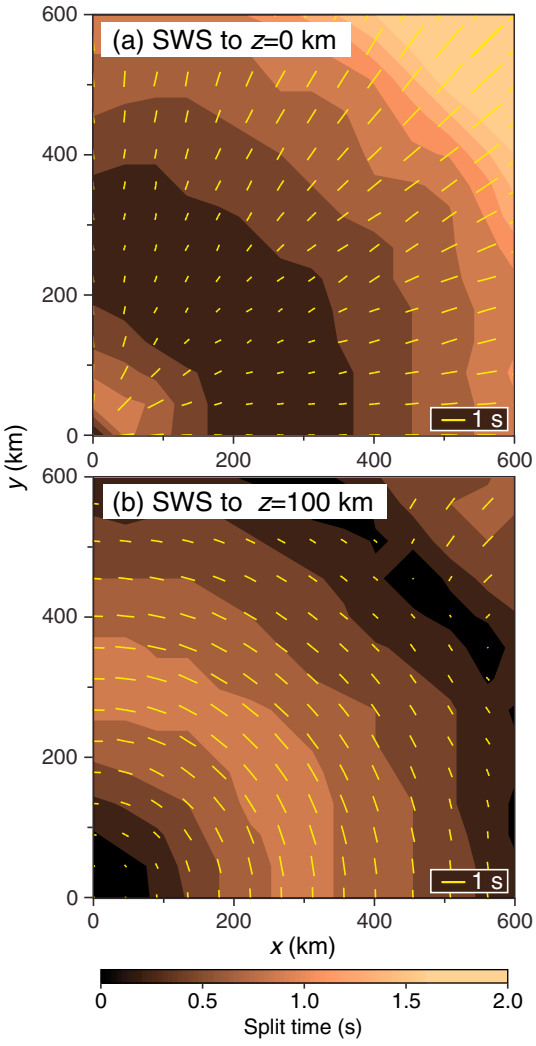


**Figure 3.** Maps of shear wave splitting (SWS) for Model SP1. (a) SWS at the surface is controlled primarily by the radial shear within and near the base of the lithosphere. (b) SWS accumulated from a depth of 200 km up to 100 km depth is controlled by the circumferential stretching in the middle-to-lower part of the plume layer. Fast polarization directions are indicated by bars; split time is indicated by length of bars and colors.

### 3.2. Effects of Plate Motions

The effects of plate motions are studied in three models with different plate speeds (Figure 4 and Table 1). These models simulate half of a plume with a reflecting boundary at $y = 0$. Plate motion creates an asymmetry in the *x* direction such that the plume pancake extends farther away from the plume center in the downwind side (right, $x > 0$) than to the upwind side (left, $x < 0$). Hence, the boundary of the plume pancake has a familiar parabolic form [*Sleep*, 1990].

Plate motion also causes an asymmetry in the distances from the plume center where the anisotropy switches from type II (circumferentially oriented *a* axes, again see Table 2) to type III (*a* axes tending toward direction of plume-plate shear) in the lower part of the plume pancake (~90 km below the base of the plate, Figures 4c, 4f, and 4i). Without plate motion, the pattern is axisymmetric, with type II dominating within ~200 km of the plume center and type III dominating at greater distances (Figure 4c). With very slow plate motion (2.5 km/Myr, Figure 4f) and then moderate motion (20 km/Myr, Figure 4i) the switch from types II to III appears increasingly proximal to the plume center on the upwind side and more distal on the downwind side. This result reflects the increasing (decreasing) importance of plate shear on the upwind (downwind) side of the plume with increasing plate speed. At ~20 km below the plate, the olivine *a* axes everywhere become more parallel to plate motion, hence more like type III anisotropy, as plate speed is increased (Figures 4b, 4e, and 4h). The relationships between the directions of mantle flow, accumulated extension, and the *a* axes again vary strongly with position.

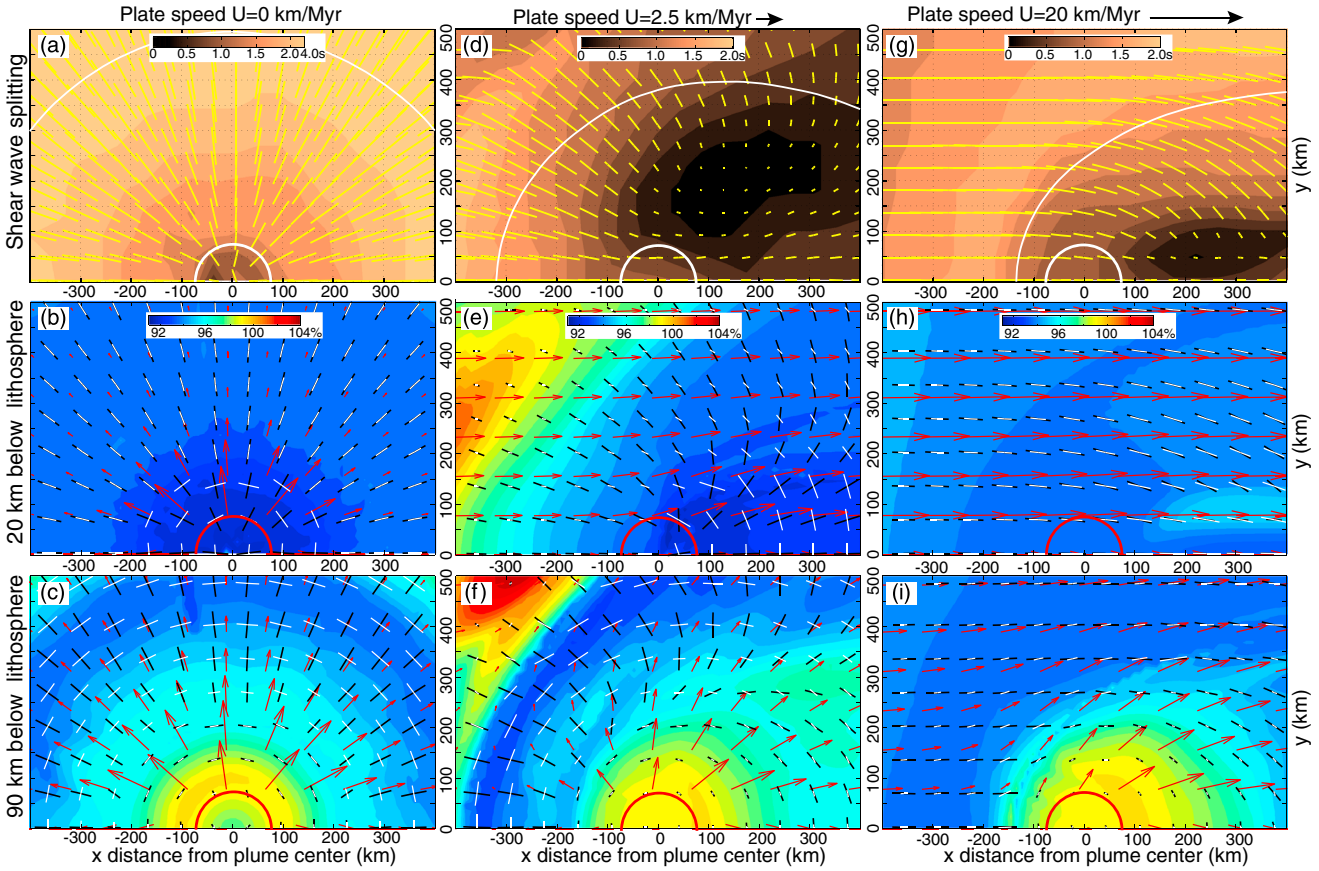


**Figure 4.** Intraplate plumes subject to different plate speeds: (a–c) fixed plate (Model SP2), (d–f) 2.5 km/Myr (Model IP1), and (g–i) 20 km/Myr (Model IP2) to the right. Predicted shear wave splitting at the surface displayed as in Figure 3 are shown in the top row. Anisotropy in horizontal cross sections at depths of 20 km (middle row) and 90 km (bottom row) below the base of the lithosphere (defined by the 1100°C isosurface) is depicted as radial anisotropy ($V_{SV}/V_{SH}$ in %, blue to red) and directions of fast $V_P$ projected onto the planes (black bars, length proportional in-plane magnitude). Also shown are in-plane directions of long axes of finite strain ellipses (white bars) and mantle velocities (red arrows). Semicircle denotes the location and radius, $r_p$, of the imposed plume stem, white arcs in Figures 4a, 4d, and 4g mark the edge of the plume pancake. Green-to-red region in the upper left corner in Figures 4e and 4f is due to a sublithospheric downwelling and should not be considered to be a general aspect of intraplate plume-plate interaction.

The pattern of SWS also reflects the differing importance of plate shear on either side of the plume stem (Figures 4a, 4d, and 4g). For the very slow moving plate, the fast polarization directions on the upwind side are angled toward, but oblique to, plate motion; on the downwind side they tend to be orthogonal to ($x > 0$, $y >$ ~200 km), or angled toward plate motion ($x > 0$, $y <$ ~200 km), and the split times are relatively small (Figure 4d). For the faster moving plate, the fast directions on the upwind side nearly parallel plate motion and on the downwind side show the circumferential pattern related to the reduced plate shear on this side. Thus, with appreciable plate speed, the fast directions form a pattern of nested U shapes that open in the direction opposite plate motion and close on the downwind side. The U shapes are roughly a mirror reflection (in the $x$ direction) of the parabolic form of the plume pancake (which closes on the upwind side and opens in the direction of plate motion on the downwind side, Figure 4g).

### 3.3. Case Example 1: Eifel Hot Spot

Our model predictions can be used to interpret observed splitting measurements at hot spots. The Eifel hot spot is one where relatively dense SWS measurements have been made over a broad area and where they have been interpreted in terms of plume-plate interaction [*Walker et al.*, 2005]. *Walker et al.* [2005] interpreted the fast polarization directions as paralleling the "parabolic" flow lines predicted for a plume being sheared by WSW plate motion, consistent with the SW motion of the Eurasian plate relative to the hot spot reference frame of the HS3-NUVEL 1A global plate motion model [*Gripp and Gordon*, 2002] (Figure 5).

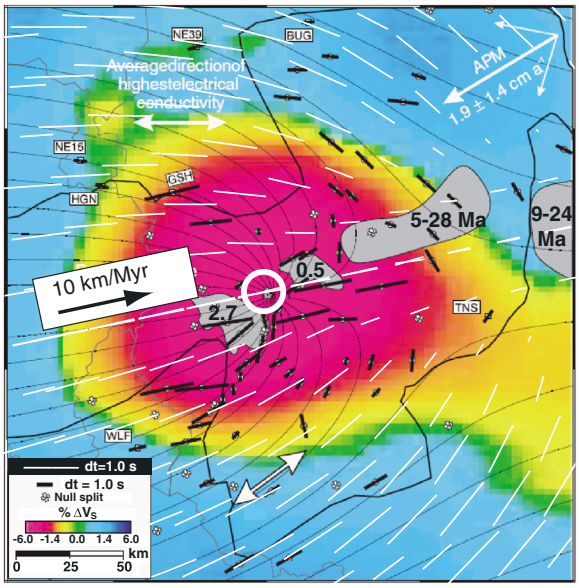


**Figure 5.** Map of the Eifel hot spot region, modified from *Walker et al.* [2005]. Assuming that fast polarization directions parallel mantle flow *Walker et al.* [2005] interpreted their shear wave splitting results (black bars) as revealing the flow of a plume being sheared by plate motion to the WSW (thin black curves show their mantle streamlines; white arrow shows absolute plate motion, APM, from *Gripp and Gordon* [2002]). In contrast, our predicted fast polarization directions (white bars) generally match the observations with a plume (centered at white circle) being sheared by ENE plate motion (large black arrow). The lateral dimensions of the predicted pattern have been reduced by 50% compared to the actual model output (Model IP3), and the largest predicted split times (~2 s) are about half of the largest observed split time (see two scales of bar length). Colors show isotropic *S* wave velocity heterogeneity at 30–100 km depth [*Keyser et al.*, 2002]; small numbers show the range of K-Ar ages in Ma compiled by *Walker et al.* [2005] within the volcanic fields denoted by gray patches.

With our models predicting that fast directions do not follow but instead are a mirror reflection of the parabolic plume flow, we find the SWS observations to be well explained by a plume interacting with a plate moving in the opposite direction or ENE (Figure 5). A moderate rate of eastward Eurasian plate motion would imply that the net westward rotation of all the plates is slower than predicted by HS3-NUVEL 1A. Indeed, the global distribution of surface wave (radial and azimuthal) anisotropy as well as SWS measurements can be best explained if the net rotation of the plates is ≤ ~50% of that of HS3-NUVEL 1A [*Becker*, 2008; *Keemer*, 2009; *Conrad and Behn*, 2010]. The match of the current model predictions to the regional SWS pattern at the Eifel hot spot requires slower net westward rotation by a comparable amount: net rotation < ~55% of that of HS3-NUVEL 1A is needed for eastward plate motion at the Eifel hot spot.

### 3.4. Case Example 2: Hawaii

Hawaii is another hot spot where shear wave splitting has been measured over a broad area. The measurements by *Collins et al.* [2012] on the Hawaiian Islands and the surrounding seafloor swell show fast polarization directions that are predominantly WSW-ENE, approximately parallel to the Molokai fracture zone (Figure 6) and roughly perpendicular to seafloor isochrons. This result was interpreted as dominantly reflecting LPO preserved in the oceanic lithosphere aligned with the fossil spreading direction. *Collins et al.* [2012] also noted some variability in the split times and directions, which they suggested could be related to a different pattern of LPO in the asthenosphere, among other possibilities.

We simulate a plume with a Hawaiian [*Ribe and Christensen*, 1999] buoyancy flux (3.8 Mg/s) interacting with a fast-moving plate (90 km/Myr) [*Gripp and Gordon*, 2002] (Model IP4). The accumulated SWS in the asthenosphere shows the previously identified pattern of nested U shapes opening against plate motion (Figure 6a). To simulate fossil LPO, we then add a lithosphere (potential temperature < ~1100°C) on top of the asthenosphere in which the olivine *a* axes preferentially align 50° from the model (present-day) plate motion. The strength of anisotropy is such that the fast *S* wave travels ~4.3% faster than the slow *S* wave across the ~90 km thick lithosphere. The predicted pattern of SWS due to both plume-plate interaction in the asthenosphere and fossil LPO in the lithosphere shows a more complex and asymmetric pattern (Figure 6b). Where the fast polarization directions due to splitting in the asthenosphere approximately align with those in the lithosphere, the split times are large, and fast directions roughly parallel the fossil LPO (e.g., 200 km < $y$ < 500 km, downwind of the plume stem). Correspondingly, where the fast directions due to splitting from the asthenosphere differ from those from the lithosphere, the split times are small, and fast directions are more variable (e.g., $x$ < 100 km, $y$ < 0).

Rotating the model so the simulated plate motion parallels the Hawaiian chain, we directly compare the predictions with observations (Figure 6c). Thirty-six (74%) of the observed fast directions are matched by the model within 19.2° (the standard deviation of the observed directions). By comparison, 33 (~68%) of the observed

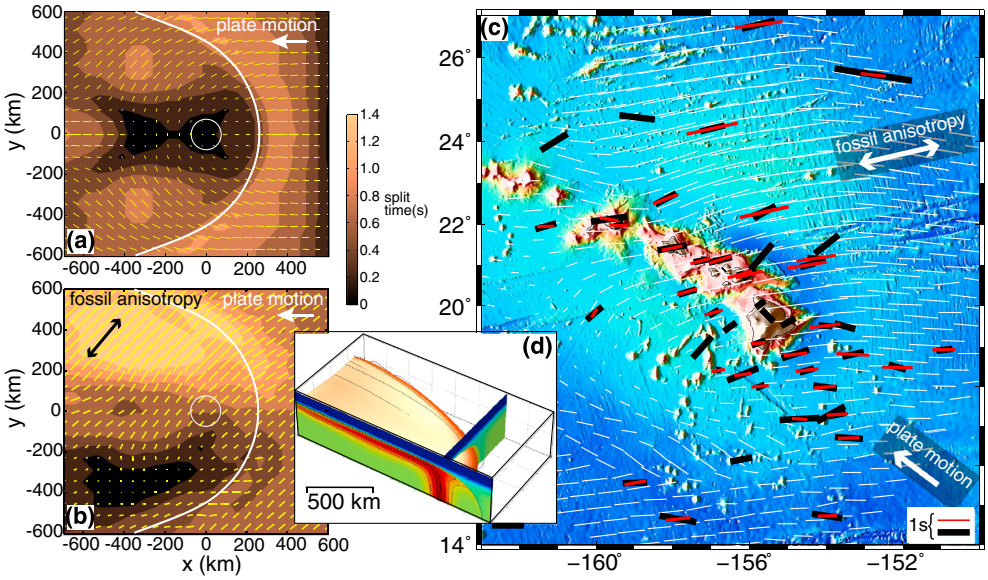


**Figure 6.** Model of the Hawaiian plume. (a) Model shear wave splitting due to mantle flow in the asthenosphere (splitting accumulated over 200–100 km depths) beneath a fast-moving (90 km/Myr) lithospheric plate (Model IP4). Circle denotes radius and location of plume stem; white curve marks boundary of sheared plume pancake. (b) SWS at the surface including the added effects of fossil LPO, simulated with by imposing a lithospheric layer (i.e., $T_p < 1100$°C) with olivine *a* axes preferentially parallel to the black double arrow. (c) The results from Figure 6b are displayed as white bars on a bathymetry map of the Hawaiian hot spot (http://topex.ucsd.edu/sandwell [*Smith and Sandwell*, 1997], illuminated from the west). Red bars show predicted fast directions that fit within a standard deviation (19.2°) of those measured by *Collins et al.* [2012] (black bars). Model plate motion and fossil LPO are indicated by large white arrows. (d) Perspective view of model plume showing two vertical cross sections of temperature (red is hot; blue is cool) and the 1360°C isosurface, illuminated from the upper left.

fast directions are matched by the model of fossil LPO only, in which the fast polarization direction in the lithosphere is the mean observed azimuth of 76° [*Collins et al.*, 2012]. Whereas slightly more predictions of the model of the plume + fossil LPO match the observations within 19.2°, the RMS misfit of this model of 19.8° is slightly greater than that (19.2°) of the fossil LPO-only model. The quality of fit between the two models is thus indistinguishable. Nonetheless, this initial comparison suggests that LPO due to plume-plate interaction, in addition to fossil LPO in the lithosphere, is influencing the SWS around Hawaii.

The above analysis is incomplete, namely because neither the plume + fossil LPO model nor fossil LPO-only model was formally optimized. The relative strength of fossil versus asthenospheric LPO is an important, unconstrained variable that was not examined. In addition, an improved model of the lithosphere should include a slight variation in fossil LPO direction as evident in the changing direction of seafloor fabric over the study area (e.g., the fabric is approximately N-S east of the chain, south of the Molokai fracture zone, and slightly more NNW-SSE, north of the fracture zone, Figure 6c). The above factors should be considered to more definitively determine the origin of the SWS around the Hawaiian hot spot.

## 4. Results: Plume-Ridge Interaction

### 4.1. Predicted Anisotropy and Shear Wave Splitting

We now consider the effects of two spreading plates, with the axis of spreading directly over the plume center. Three models are used to simulate different flow types that have previously been associated with plume-ridge interaction. The first model (RC1) is like previously published models [e.g., *Ribe et al.*, 1995] in which the viscosity is pressure- and temperature-dependent and the plates are spreading at a rate of 10 km/Myr, appropriate for the Mid-Atlantic Ridge (MAR) near Iceland (Figure 7a). The second model (RC2) simulates an artificially slow spreading rate (1 km/Myr), which leads to strong channeled flow of the plume along the ridge axis [*Fu et al.*, 2012; *Gallego et al.*, 2013] as originally conceived by *Vogt* [1971] (Figure 7b). The third model (RC3) includes the additional effects of water on viscosity, thus simulating high viscosities above the dry solidus [*Ito et al.*, 1999; *Bianco et al.*, 2013] (Figure 7c). In all cases, the plume is centered at $x = y = 0$, the ridge axis is at $x = 0$, and the side boundaries at $x = 0$ and $y = 0$ are reflecting.

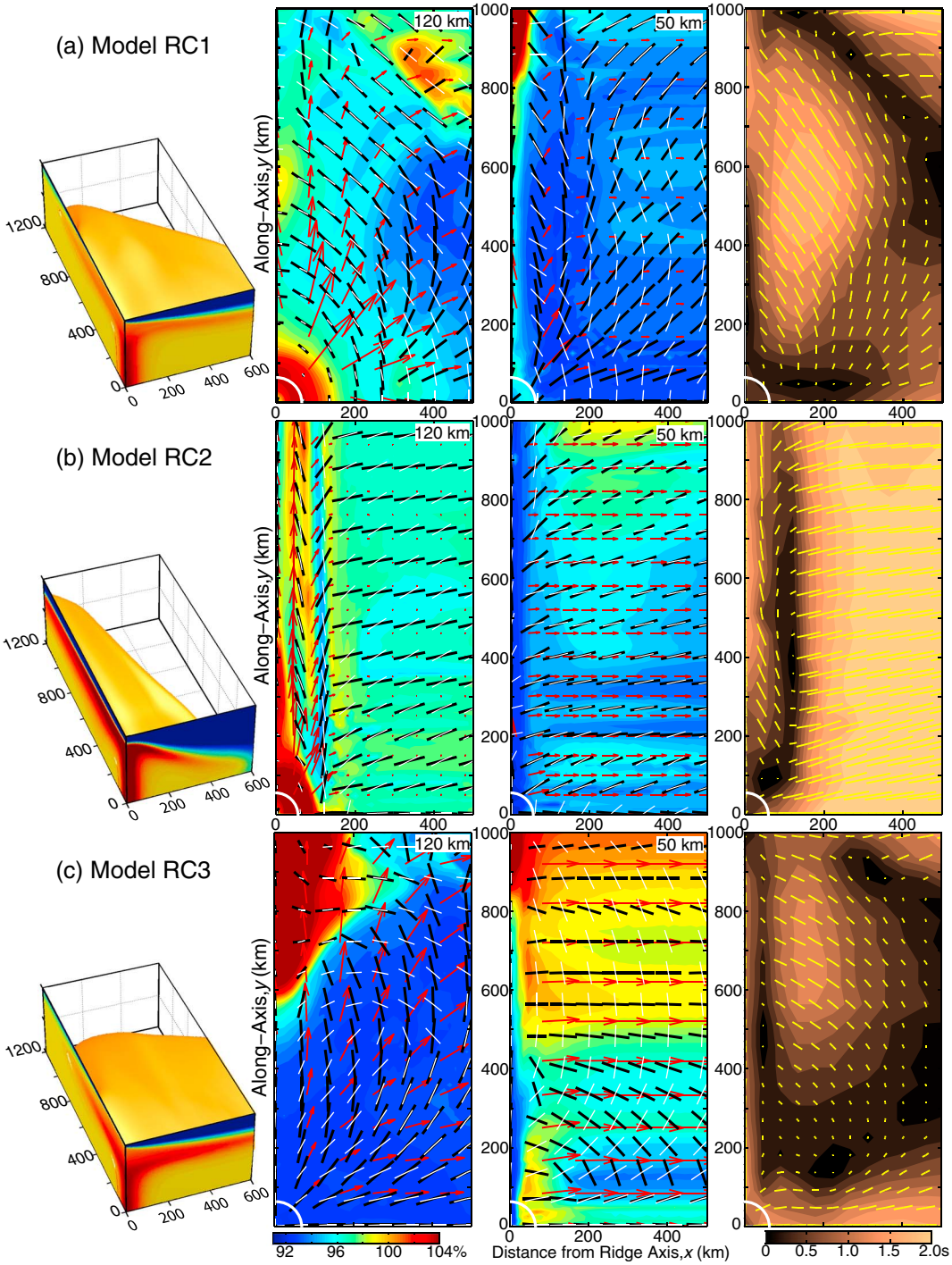


**Figure 7.** Ridge-centered plume models. The three rows show (a) Model RC1 with a plume centered beneath a mid-ocean ridge, spreading at 10 km/Myr; (b) Model RC2 of a plume centered beneath a ridge spreading at 1 km/Myr; and (c) Model RC3 which is much like RC1 but includes the effects of dehydration, which creates high viscosities in the dry melting zone. Three-dimensional perspective view of potential temperatures (colored) in vertical cross sections at $x = 0$ and $y = 0$ and the 1360°C isosurface (first column). Predicted anisotropy in horizontal planes at depths of 120 km and 50 km displayed as in Figure 4 (second and third columns). Predicted SWS displayed as in Figure 3 (fourth column). White quarter circles denote location and radius, $r_p$, of imposed plume stem.

Model RC1, with an MAR-like spreading rate, predicts the plume to spread in all directions away from the plume center, but slightly faster, parallel to the ridge axis at a depth of 120 km, well below the lithosphere (Figure 7a). At this depth, in the rising plume stem (within ~150 km of the plume center), type I anisotropy ($V_{SV}/V_{SH} > 1$) is apparent. At 120 km depth surrounding the plume stem (radial distances 150 to ~ 300 km), type II anisotropy ($V_{SV}/V_{SH} < 1$ circumferentially oriented *a* axes) is apparent. Moving along the ridge axis to increasing *y* (and $x \leq 300$ km), the *a* axes slant diagonally toward the ridge at a large angle from the flow direction and parallel to the long axes of the FSEs. This "type IV" anisotropy (Table 2) reflects an appreciable component of *x*-*y* shear because the along-axis component of flow is fastest directly beneath the ridge axis ($x = 0$) and decreases with *x* away from the ridge axis. At a depth of 50 km, along-axis plume flow is confined to a distance of $x <$ ~ 200 km of the ridge; for $x \geq 200$ km, the lithosphere is encountered and the flow is directly away from the ridge at the plate speed. At this depth the *a* axes are mostly in the horizontal plane, as indicated by $V_{SV}/V_{SH} < 1.0$. Within a radial distance of ~400 km of the plume center, the olivine *a* axes are oriented radially away from the plume center; thus, the anisotropy resembles type III (heavily influenced by plume-plate shear). At $y >$ ~400 km type IV anisotropy (*a* axes angled toward the ridge) is apparent over a relatively narrow band ($x <$ ~100 km) near the ridge axis. The predicted pattern of SWS (at the surface of the model) displays fast directions dominantly oriented diagonally toward the ridge axis where $x <$ ~200 km and $y >$ ~100 km, largely reflecting the type IV anisotropy. Along the symmetry line of $y = 0$ the fast directions parallel plate motion.

In the second model (RC2), the ultraslow spreading rate causes the plate to thicken very rapidly away from the ridge and confine the plume to an along-axis channel, which is ~300 km wide at 200 km depth and narrows with decreasing depth (Figure 7b). At a depth of 120 km, the along-axis plume channel is ~130 km wide within which the flow is primarily ridge parallel. Type IV anisotropy is prevalent in this zone. In the lithosphere ($x >$ ~130 km), the olivine *a* axes are oriented at a large angle away from the ridge axis at 120 km depth. At a depth of 50 km, the plume channel is $<$ 30 km wide. Thus, the *a* axes are already oriented away from the ridge axis at *x* ~30 km and are mostly horizontal ($V_{SV}/V_{SH} < 1.0$). SWS is predicted to show fast polarization directions that angle toward the ridge axis within ~ 100 km of it (reflecting type IV anisotropy) and are directed away from the ridge axis where $x >$ ~150 km. Thus, the pattern of SWS reveals an apparent plume channel that is 100–150 km wide or about half its maximum width in the upper ~200 km. The fast polarization directions parallel the ridge axis only directly beneath it, not generally elsewhere in the region of the plume channel.

In the third model (RC3), which has a MAR-like spreading rate and includes the effects of water on viscosity, the dehydrated layer behaves as a stiff, compositional lithosphere that is relatively thick (average of ~100 km where the ridge is underlain by plume material) and does not thicken away from the ridge axis like the thermal lithosphere (Figure 7c). At 120 km depth within a radial distance of ~300 km of the plume center, mantle flow, the long axes of the FSEs, and the *a* axes generally radiate away from the plume center, reflecting type III anisotropy. The anisotropy at 120 km depth crudely resembles that of RC1 at 50 km depth, the two depths being near the base of the stiff lithosphere in each model. At a depth of 50 km in model RC3, viscosities are high and the flow is essentially equal to plate motion. The *a* axes generally align with plate motion in this plane but also have a large vertical component as indicated by $V_{SV}/V_{SH} \geq 1.0$. A local peak in $V_{SV}/V_{SH}$ occurs just to the side of the ridge axis near $x = 50$ km at 50 km depth. In *x*-*z* cross section (not shown), this peak in $V_{SV}/V_{SH}$ is very close to the ridge axis near the surface and extends diagonally down and away from the ridge at ~45° from vertical. *Gallego et al.* [2013] showed that this diagonal feature tends to produce negative radial anisotropy ($[V_{SH} - V_{SV}]/[(V_{SH} + V_{SV})/2] < 0$) on the side of the ridge axis in inversions of synthetic surface wave phase velocities and that this negative anisotropy crudely resembles that imaged on the sides of the Reykjanes Ridge near Iceland [*Delorey et al.*, 2007]. The split times predicted by model RC3, overall, are relatively small. The largest split times occur near the symmetry plane at $y = 0$, where the fast directions are nearly parallel to plate motion, and in the area of $50 < x < 250$, $500 < y < 900$, where the fast directions are angled toward the ridge axis.

### 4.2. Case Example 3: Iceland

Comparisons of the predicted SWS patterns and observations on Iceland are made by reflecting the models about the symmetry planes at $x = 0$ and $y = 0$ and projecting them in geographic coordinates, with the model and actual spreading directions aligned and the plume centered on Vatnajökull glacier [e.g., *Wolfe et al.*, 1997] (Figure 8).

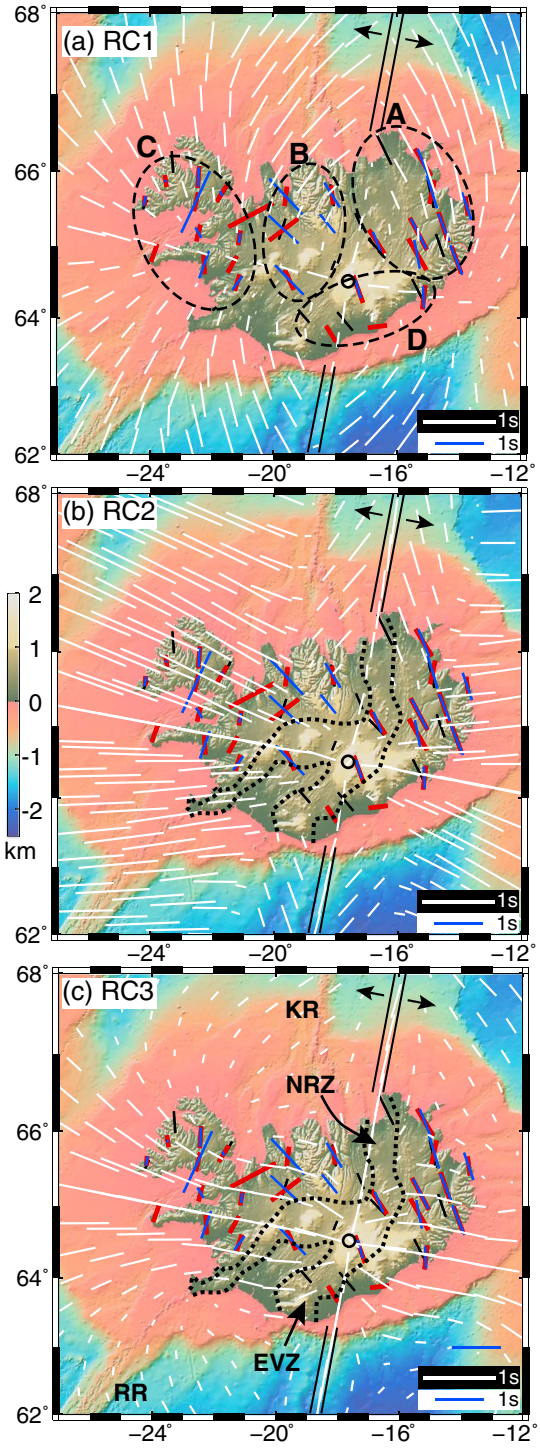


**Figure 8.** Topography map of Iceland overlain with observed *S* wave splitting results of *Bjarnason et al.* [2002] (black bars), *Li and Detrick* [2003] (red bars), and *Xue and Allen* [2005] (blue bars). These are compared with predictions (white bars) of Models (a) RC1, (b) RC2, and (c) RC3. Bar length is proportional to split time but scaled differently between observations and predictions as indicated in the legend. Dotted curves outline zones of active rifting. Model ridge axis is marked by double solid lines outside of Iceland, model spreading direction is shown by paired arrows, and plume center is marked by small black circles. NRZ = Northern Rift Zone, EVZ = Eastern Volcanic Zone, KR = Kolbeinsey Ridge, and RR = Reykjanes Ridge. Letters A, B, C, and D distinguish groups of observed fast polarization directions surrounded by dashed ellipses.

The models are only a crude representation of the Iceland-MAR system, especially given that the real plate boundary is not perfectly straight but deviates on Iceland some 200 km to the east of the Reykjanes and Kolbeinsey Ridges, south and north of Iceland, respectively.

Supporting our prior results [*Fu et al.*, 2012], the models of a low-viscosity plume (here RC1 and RC2) predict NNW-SSE fast polarization directions in eastern Iceland (zone A, Figure 8), generally consistent with those observed. The reference model RC1 with a realistic spreading rate (10 km/Myr, like models GM2 and GM4 of *Fu et al.* [2012]) produces the better match to the observations in eastern Iceland because it predicts the NNW-SSE pattern to extend farther east of the ridge axis than the model RC2 of artificially strong, along-axis plume channeling (same as model GM3 of *Fu et al.* [2012]). Model RC3 with a high-viscosity, dehydrated layer corresponding to the dry melting zone predicts fast directions that are variable and more E-W in eastern Iceland and thus produces the poorest match to the observed fast directions in eastern Iceland (Figure 8c). Model RC1—unlike RC2 and RC3—also predicts directions moderately consistent with the N-S fast directions observed in the far western part of Iceland (zone C, Figure 8a). None of the models predict the NNW-SSE fast directions just west of the Northern Rift Zone (zone B) and in the Eastern Volcanic Zone (zone D) south of the plume center. Thus, if the shear wave splitting is controlled primarily by LPO of olivine A-type fabric in the Icelandic upper mantle, these results suggest a type of plume flow like that of model RC1: one involving a low-viscosity plume below the thermal lithosphere.

Model RC3 produces the least favorable match to the shear wave splitting on Iceland, and this result contradicts those of prior studies that argue in favor of a dehydrated and high-viscosity layer for explaining crustal thickness [*Ito et al.*, 1999] as well as geochemical [*Bianco et al.*, 2013] variations on Iceland and along the MAR. The result also contradicts *Gallego et al.*'s [2013] suggestion that a high-viscosity shallow layer contributes to (but does not produce an adequate explanation for) the aforementioned negative radial anisotropy on the sides of the Reykjanes Ridge [*Delorey et al.*, 2007]. Hence, a reexamination of both types of models (RC1 and RC3) is needed in future studies. In particular, a more realistic ridge geometry and plate motion may be important to the various observations, especially SWS. In addition, the rheology simulated here, as well as previously [*Ito et al.*, 1999; *Bianco et al.*, 2013], is only approximate in that stress and strain rate are linearly related. A more realistic power law relationship, associated with dislocation creep, can reduce the effective viscosities where strain rates are high near the ridge axis and lead to variable thickness of the anisotropic layer [*Conder*, 2007], which together should be important to the SWS.

## 5. Conclusions

Geodynamic models of mantle convection and the evolution of LPO in olivine-enstatite aggregates, assuming olivine A-type fabric, are used to investigate the patterns of seismic anisotropy associated with plume-plate interaction. The preferred orientation of the olivine *a* axis is predicted to show spatially variable relationships to the directions of mantle flow and accumulated extensional strain. Within the upwelling plume stem, the *a* axes are near vertical (type I anisotropy). In the deeper half of the layer of plume material ponding beneath the lithosphere, the *a* axes tend to orient perpendicular to the radial flow of the plume; they form circular patterns around the plume stem, reflecting circumferential stretching (type II anisotropy). Shallower in the plume layer, shear near the base of the lithosphere becomes important and the *a* axes begin to orient toward the shear direction between the plume and plate (type III anisotropy).

For an intraplate plume rising beneath a moving plate, the predicted pattern of shear wave splitting reflects a greater amount shear between the plate and plume on the upwind side of the plume with fast polarization directions tending to parallel plate motion (type III anisotropy), whereas on the downwind side of the plume, the shear between the plate and plume is less, and fast directions tend to be circumferentially oriented (type II anisotropy). The pattern of fast polarization directions is that of a series of nested U shapes that open into the mantle wind not away from it, which is opposite the parabolic shape used to describe the plume flow lines. The predicted SWS pattern matches the observed pattern around the Eifel hot spot reasonably well if the Eurasian plate is moving eastward. An eastward, rather than westward, absolute plate motion is consistent with prior studies that best explain global patterns of seismic anisotropy with slower net (westward) rotation of all the plates than represented by HS3-NUVEL 1A. Around the Hawaiian hot spot, SWS appears to be heavily influenced by fossil LPO in the lithosphere, but models show promise for the additional effects of LPO in the asthenosphere due to plume-plate interaction as also being important.

For a ridge-centered plume rising beneath two plates diverging at a realistically slow rate (10 km/Myr) (Model RC1), fast polarization directions of SWS orient roughly circumferentially around the plume stem (type II anisotropy) and angle diagonally toward the ridge axis (type IV anisotropy). This pattern better matches the observed pattern in eastern and far western Iceland than a model in which the plume is confined to a narrow (~300 km at maximum width) channel along the ridge axis (Model RC2) or a model that includes a high-viscosity dehydrated layer in the shallowest upper mantle (Model RC3). None of the models, however, adequately explain the full pattern of SWS on Iceland.

**Acknowledgments**

We thank Clint Conrad for making us aware of the issues related to the rate of net plate rotation and the direction of the Eurasian plate motion. We owe much of our time saved to Karen Fischer and David Abt for providing us with their MATLAB codes for simulating shear wave splitting and solving for the splitting parameters. Reviews by the Associate Editor, Derek Schutt, and an anonymous reviewer were valuable, especially in helping us clarify various aspect of this study. This project was funded by NSF grants 0855814 to Ito, Dunn, and Gallego, and 0855767 to Li. Contact Garrett Ito (gito@hawaii.edu) for access to all computer codes use for this project. This is SOEST contribution 9095.

## References

Barruol, G., and F. R. Fontaine (2013), Mantle flow beneath La Réunion hotspot track from SKS splitting, *Earth Planet. Sci. Lett.*, *362*, 108–121.

Becker, T. W. (2008), Azimuthal seismic anisotropy constrains net rotation of the lithosphere, *Geophys. Res. Lett.*, *35*, L05303, doi:10.1029/2007GL032928.

Becker, T. W., S. Chevrot, V. Schulte-Pelkum, and D. K. Blackman (2006), Statistical properties of seismic anisotropy predicted by upper mantle geodynamic models, *J. Geophys. Res.*, *111*, B08309, doi:10.1029/2005JB004095.

Bianco, T. A., G. Ito, J. van Hunen, J. J. Mahoney, and M. D. Ballmer (2013), Geochemical variations at ridge-centered hotspots caused by variable melting of a veined mantle plume, *Geochem. Geophys. Geosyst.*, *371*, 191–202, doi:10.1016/j.epsl.2013.03.050.

Bjarnason, I. T., P. G. Silver, G. Rumpker, and S. C. Solomon (2002), Shear wave splitting across the Iceland hot spot: Results from the ICEMELT experiment, *J. Geophys. Res.*, *107*(B12), 2382, doi:10.1029/2001JB000916.

Blackman, D. K. (2007), Use of mineral physics, with geodynamic modelling and seismology, to investigate flow in the Earth's mantle, *Rep. Prog. Phys.*, *7*, 659–689.

Blackman, D. K., and J. M. Kendall (1997), Sensitivity of teleseismic body waves to mineral texture and melt in the mantle beneath a mid-ocean ridge, *Philos. Trans. R. Soc. London, Ser. A*, *355*(1723), 217–231.

Castelnau, O., D. K. Blackman, and T. W. Becker (2009), Numerical simulations of texture development and associated rheological anisotropy in regions of complex mantle flow, *Geophys. Res. Lett.*, *36*, L12304, doi:10.1029/2009GL038027.

Collins, J. A., C. J. Wolfe, and G. Laske (2012), Shear wave splitting at the Hawaiian hot spot from the PLUME land and ocean bottom seismometer deployments, *Geochem. Geophys. Geosyst.*, *13*, Q02007, doi:10.1029/2011GC003881.

Conder, J. (2007), Dynamically driven mantle flow and shear wave splitting asymmetry across the EPR, MELT area, *Geophys. Res. Lett.*, *34*, L16301, doi:10.1029/2007GL030832.

Conrad, C. P., and M. Behn (2010), Constraints on lithosphere net rotation and asthenospheric viscosity from global mantle flow models and seismic anisotropy, *Geochem. Geophys. Geosyst.*, *11*, Q05W05, doi:10.1029/2009GC002970.

Conrad, C. P., M. D. Behn, and P. G. Silver (2007), Global mantle flow and the development of seismic anisotropy: Differences between the oceanic and continental upper mantle, *J. Geophys. Res.*, *112*, B07317, doi:10.1029/2006JB004608.

Delorey, A., R. A. Dunn, and J. B. Gaherty (2007), Surface wave tomography of the upper mantle beneath the Reykjanes Ridge with implications for ridge-hotspot interaction, *J. Geophys. Res.*, *112*, B08313, doi:10.1029/2006JB004785.

Druken, K. A., C. R. Kincaid, and R. W. Griffiths (2013), Directions of seismic anisotropy in laboratory models of mantle plumes, *Geophys. Res. Lett.*, *40*, 3544–3549, doi:10.1002/grl.50671.

Fischer, K. M., E. M. Parmentier, A. R. Stine, and E. R. Wolfe (2000), Modeling anisotropy and plate-driven flow in the Tonga subduction zone back arc, *J. Geophys. Res.*, *105*, 16,181–16,191, doi:10.1029/1999JB900441.

Fontaine, F. R., E. E. E. Hooft, P. G. Burkett, D. R. Toomey, S. C. Solomon, and P. G. Silver (2005), Shear-wave splitting beneath the Galapagos archipelago, *Geophys. Res. Lett.*, *32*, L21308, doi:10.1029/2005GL024014.

Fontaine, F. R., G. Barruol, A. Tommasi, and G. H. R. Bokelmann (2007), Upper-mantle flow beneath French Polynesia from shear wave splitting, *Geophys. J. Int.*, *170*, 1262–1288.

Fu, Y., A. Li, and G. Ito (2012), Waveform modeling of shear wave splitting from anisotropic models in Iceland, *Geochem. Geophys. Geosyst.*, *13*, Q12001, doi:10.1029/2012GC004369.

Gaboret, C., A. M. Forte, and J. P. Montagner (2003), The unique dynamics of the Pacific Hemisphere mantle and its signature on seismic anisotropy, *Earth Planet. Sci. Lett.*, *208*(3–4), 219–233.

Gallego, A., G. Ito, and R. Dunn (2013), Investigating seismic anisotropy beneath the Reykjanes Ridge using models of mantle flow, crystallographic evolution, and surface wave propagation, *Geochem. Geophys. Geosyst.*, *14*, 3250–3267, doi:10.1002/ggge.20204.

Gripp, A. E., and R. G. Gordon (2002), Young tracks of hotspots and current plate velocities, *Geophys. J. Int.*, *150*, 321–361.

Hirth, G., and D. L. Kohlstedt (1996), Water in the oceanic upper mantle: Implications for rheology, melt extraction, and the evolution of the lithosphere, *Earth Planet. Sci. Lett.*, *144*, 93–108.

Holtzman, B. K., and J.-M. Kendall (2010), Organized melt, seismic anisotropy, and plate boundary lubrication, *Geochem. Geophys. Geosyst.*, *11*, Q0AB06, doi:10.1029/2010GC003296.

Holtzman, B. K., D. L. Kohlstedt, M. E. Zimmerman, F. Heidelbach, T. Hiraga, and J. Hustof (2003), Melt segregation and strain partitioning: Implications for seismic anisotropy and mantle flow, *Science*, *301*, 1227–1230.

Ito, G., Y. Shen, G. Hirth, and C. Wolfe (1999), Mantle flow, melting, and dehydration of the Iceland mantle plume, *Earth Planet. Sci. Lett.*, *165*, 81–96.

Jung, H., and S. Karato (2001), Water-induced fabric transitions in olivine, *Science*, *293*, 1460–1463.

Kaminski, E., and N. M. Ribe (2001), A kinematic model for recrystallization and texture development in olivine polycrystals, *Earth Planet. Sci. Lett.*, *189*, 253–267.

Kaminski, E., and N. M. Ribe (2002), Timescales for the evolution of seismic anisotropy in mantle flow, *Geochem. Geophys. Geosyst.*, *3*(8), Q01051, doi:10.1029/2001GC000222.

Kaminski, È., N. M. Ribe, and J. T. Browaeys (2004), D-Rex, a program for calculation of seismic anisotropy due to crystal lattice preferred orientation in the convective upper mantle, *Geophys. J. Int.*, *158*, 744–752.

Karato, S. (1992), On the Lehmann discontinuity, *Geophys. Res. Lett.*, *19*(22), 2255–2258, doi:10.1029/92GL02603.

Karato, S. (2007), Geodynamic significance of seismic anisotropy of the upper mantle: New insights from laboratory studies, *Annu. Rev. Earth Planet. Sci.*, *36*, 59–95.

Karato, S., and P. Wu (1993), Rheology of the upper mantle: A synthesis, *Science*, *260*, 771–778.

Keemer, C. (2009), Absolute plate motions constrained by shear wave splitting orientations with implications for hot spot motions and mantle flow, *J. Geophys. Res.*, *114*, B10405, doi:10.1029/2009JB006416.
Keyser, M., J. R. R. Ritter, and M. Jordan (2002), 3D shear-wave velocity structure of the Eifel plume, Germany, *Earth Planet. Sci. Lett.*, *203*, 59–82.
Li, A., and R. S. Detrick (2003), Azimuthal anisotropy and phase velocity beneath Iceland: Implication for plume-ridge interaction, *Earth Planet. Sci. Lett.*, *214*, 153–165.
Mainprice, D. (1997), Modeling the anisotropic seismic properties of partially molten rocks found at mid-ocean ridges, *Tectonophysics*, *279*, 161–179.
Marquart, G., H. Schmeling, and O. Cadek (2007), Dynamic models for mantle flow and seismic anisotropy in the North Atlantic region and comparison with observations, *Geochem. Geophys. Geosyst.*, *8*, Q02008, doi:10.1029/2006GC001359.
Moresi, L. N., and M. Gurnis (1996), Constraints on the lateral strength of slabs from three dimensional dynamic flow models, *Earth Planet. Sci. Lett.*, *138*, 15–28.
Nicholas, A., and N. I. Christensen (1987), Formation of anisotropy in upper mantle peridotites: A review, in *Composition, Structure and Dynamics of the Lithosphere-Asthenosphere System*, *Geodyn. Monogr. Ser.*, edited by K. Fuchs and C. Froidevaux, pp. 111–123, AGU, Washington, D. C.
Ribe, N. (1989), A continuum theory for lattice preferred orientation, *Geophys. J.*, *97*, 199–207.
Ribe, N. (1992), On the relation between seismic anisotropy and finite strain, *J. Geophys. Res.*, *97*, 8737–8747, doi:10.1029/92JB00551.
Ribe, N. M., and U. R. Christensen (1999), The dynamical origin of Hawaiian volcanism, *Earth Planet. Sci. Lett.*, *171*, 517–531.
Ribe, N., U. R. Christensen, and J. Theissing (1995), The dynamics of plume-ridge interaction. 1: Ridge-centered plumes, *Earth Planet. Sci. Lett.*, *134*, 155–168.
Rümpker, G., and P. G. Silver (1998), Apparent shear-wave splitting parameters in the presence of vertically varying anisotropy, *Geophys. J. Int.*, *135*(3), 790–800.
Rümpker, G., and P. G. Silver (2000), Calculating splitting parameters for plume-type anisotropic structures of the upper mantle, *Geophys. J. Int.*, *143*(3), 507–520.
Silver, P. G., and W. W. Chan (1991), Shear-wave splitting and subcontinental mantle deformation, *J. Geophys. Res.*, *96*(B10), 16,429–16,454, doi:10.1029/91JB00899.
Sleep, N. H. (1990), Hotspots and mantle plumes: Some phenomenology, *J. Geophys. Res.*, *95*, 6715–6736, doi:10.1029/JB095iB05p06715.
Smith, W. H. F., and D. T. Sandwell (1997), Global seafloor topography from satellite altimetry and ship depth soundings, *Science*, *277*, 1957–1962.
Takeuchi, H., and M. Saito (1972), Seismic surface waves, in *Methods in Computational Physics*, edited by B. A. Bolt, Academic Press, New York.
Vogt, P. R. (1971), Asthenosphere motion recorded by the ocean floor south of Iceland, *Earth Planet. Sci. Lett.*, *13*, 153–160.
Waite, G. P., D. L. Schutt, and R. B. Smith (2005), Models of lithosphere and asthenosphere anisotropic structure of the Yellowstone hot spot from shear wave splitting, *J. Geophys. Res.*, *110*, B11304, doi:10.1029/2004JB003501.
Walker, K. T., G. H. R. Bokelmann, S. L. Klemperer, and G. Bock (2005), Shear-wave splitting around the Eifel hotspot: Evidence for a mantle upwelling, *Geophys. J. Int.*, *163*(3), 962–980.
Wenk, H. R., K. Bennet, G. Canova, and A. Molinari (1991), Modeling plastic deformation of peridotite with the self-consistent theory, *J. Geophys. Res.*, *96*, 8337–8349, doi:10.1029/91JB00117.
Wolfe, C. J., and P. G. Silver (1998), Seismic anisotropy of oceanic upper mantle: Shear wave splitting methodologies and observations, *J. Geophys. Res.*, *103*(B1), 749–771, doi:10.1029/97JB02023.
Wolfe, C., I. T. Bjarnason, J. C. VanDecar, and S. C. Solomon (1997), Seismic structure of the Iceland mantle plume, *Nature*, *385*, 245–247.
Xue, M., and R. M. Allen (2005), Asthenospheric channeling of the Icelandic upwelling: Evidence from seismic anisotropy, *Earth Planet. Sci. Lett.*, *235*(1–2), 167–182.
Zhang, S., and S. Karato (1995), Lattice preferred orientation of olivine aggregates deformed in simple shear, *Nature*, *375*, 774–777.
Zhong, S., M. T. Zuber, L. N. Moresi, and M. Gurnis (2000), The role of temperature-dependent viscosity and surface plates in spherical shell models of mantle convection, *J. Geophys. Res.*, *105*, 11,063–11,082, doi:10.1029/2000JB900003.